**Electrosynthesis of Quasi-Epitaxial Crystals on Liquid Metals**

Joshua P. Hazelnis[1] and Stephen Maldonado[1,2‡]

1. Department of Chemistry University of Michigan, 930 North University, Ann Arbor, Michigan 48109-1055

2. Program in Applied Physics, University of Michigan, 2477 Randall Laboratory, Ann Arbor, MI 48109-1040

**Abstract.**

Electrosynthesis of single-crystalline metallic and intermetallic particles with preferred orientation onto liquid metal electrodes has been performed. Liquid gallium electrodes immersed in aqueous alkaline electrolytes without any molecular additive or external solid seeding substrates were used to electroreduce separately $Pb^{2+}$, $Bi^{3+}$, $Pd^{2+}$, and $Mn^{2+}$. The crystallinity, composition, and orientation of the electrodeposition products were characterized using scanning electron microscopy, transmission electron microscopy, selected area electron diffraction, grazing incidence X-ray diffraction, and energy dispersive X-ray spectroscopy. Electrodeposition of Pb and Bi results in the incipient formation of 2D nuclei that subsequently direct the growth of Pb and Bi single-crystals along the most closed packed [111] and [0001] directions, respectively. The absence of any intervening surface oxides and low electroreduction flux are necessary to avoid polycrystalline dendrite formation. Under comparable conditions, electrodeposition of Pd and Mn results in single crystalline intermetallic particles at the interface. Each crystal exhibits a preferred orientation consistent with the unique atomic packing of the near-surface region of liquid Ga. The presented study suggests a new concept in electrodeposition processes where the liquid metal structure imparts quasi-epitaxial growth in a system where the electrode material specifically has no crystallinity or long-range order. This study is thus the first demonstration of highly oriented electrodeposition at a liquid/liquid interface at ambient conditions, highlighting the unique solvation environment of liquid metal interfaces for forming thin metallic and intermetallic films.

‡ To whom correspondence should be addressed. Phone: 734-647-4750; email: smald@umich.edu

**Introduction.**

Synthetic strategies that produce inorganic crystals with control and precision are necessary for (opto)electronic, sensing, and energy conversion technologies. Among the many current methods, strategies that leverage liquid metals as reaction media were historically among the first to be developed.[1] Resurgent interest in liquid metals has pushed their use to the forefront again, particularly for crystalline nanomaterials.[2] The general appeals of liquid metals are their physical malleability, their solvent characteristics towards inorganic solutes of interest, and the thermodynamic tendency for surface enrichment in oxides on liquid metal mixtures.

In addition to these aspects, liquid metals have one other potentially significant but otherwise under-exploited attribute. Unlike molecular liquids, liquid metals exhibit short-range atomic layering in the near surface region along the surface normal extending towards the bulk (**Figure 1**).[3-6] This atomic ordering is not crystalline per se since there is no evidence of persistent, long range, lateral ordering. Still, it is sufficient to yield a quasi-Bragg reflection at x-ray wavelengths.[6-7] The surface layering likely arises from the abrupt change in electronic structure at liquid metal interfaces with air and water.[8] For crystallization, this near-surface atomic layering is thought to explain the observation of highly anisotropic metal crystal growth observed during surface freezing of dilute liquid metal alloys under vacuum.[9-12] Presently, there is no indication that near-surface atomic layering is specifically influential in any other syntheses based on liquid metals.

Our group is generally interested in electrodepositions performed with liquid metals, where nucleation and growth of inorganic crystals is possible with electrochemical rather than thermal stimuli and can be performed in lab ambient rather than evacuated chambers.[13-14] The appeal is that electrochemical synthetic reactions can be initiated/terminated precisely with extremely simple control hardware. Several types of inorganic crystals can be prepared this way.[13-14] However, controlling their crystal type and orientation requires the presence of a separate, external solid (seed) surface.[15-16] That is, epitaxy in electrodepositions with liquid metals has thus far only been possible with an additional, non-native solid/liquid interface.

Herein, this work demonstrates a new concept in the electrosynthesis of crystalline inorganic materials. This report tests the hypothesis that it is possible to electrodeposit crystalline metals with a preferred orientation at a liquid metal electrode interface that itself has no solid

crystallinity, no external additives/binding agents in solution, and does not include an external solid seed substrate. The experiments described herein report on the separate electrodepositions of Pb, Bi, Pd, and Mn onto liquid Ga at constant, ambient temperature. The results show that when the liquid Ga/electrolyte interface is devoid of oxides, self-segregation and directed crystal growth of the metallic materials at the interface is possible. For metals that are immiscible with liquid Ga, electrodeposition under low flux conditions results in single-crystals of the metal solutes with a preferred orientation. For metals that are miscible with liquid Ga, electrodeposition at low flux conditions produces intermetallic single-crystals with a preferred orientation. In both cases, the observed crystal orientations are consistent with nucleation planes defined by the atomic packing density of atomic layers within Ga, suggesting that the intrinsic atomic structure of the near surface region of the liquid metal is key.

**Experimental.**

*Electrochemical Cell* A potentiostat (Autolab PGSTAT302N, Metrohm) and custom Teflon electrochemical cell were used for all electrochemical measurements (Figure 1a). All measurements were performed in triplicate and open to air in ambient. The working electrode was a 2.035 ± 0.007 g liquid Ga droplet (99.99999% Pure, Fisher Scientific) in contact with a Pt wire ohmic contact housed in a quartz glass capillary with a 1.30 mm diameter. A teflon bowl with a diameter of 0.90 cm and depth of 0.60 cm contained the liquid Ga (Figure 1a). The surface area of the Ga electrode in contact with the liquid electrolyte was approximately 1.89 $cm^2$ after subtraction of the area of the ohmic contact capillary (diameter = 0.13 cm).

The cell was placed on a hotplate set to $T = 65°C$ to ensure Ga remained liquid throughout the duration of the electrodeposition experiments. A platinum (Pt) wire was used as the counter electrode. A BASi alkaline Hg/HgO half cell was used as the reference electrode (1.25 M NaOH filling solution). All potentials are reported with respect to this reference. The electrolyte was 1.25 M trace metal grade NaOH (99.99%, Sigma Aldrich) which was further purified before use by presoaking a separate (sacrificial) pool of Ga at $T = 65°C$ for at least 1 week to getter metal cations. Subsequent iron levels (one of the dominant metal contaminant in alkaline salts)[17] in the electrolyte were measured from aliquots via inductively coupled plasma mass spectrometry (ICP-MS) and determined to stabilize after removing no greater than 0.08 ppm. A leach rate of 0.034 mg Ga $hr^{-1}$ was also determined experimentally via ICP-MS. This is in good agreement with previous reports

of the anodic corrosion of Ga in alkaline solutions.[18] Therefore, as a consequence of the presoaking process to getter metal cations, the electrolytes will be sufficiently saturated with Ga ions. All electrochemical data are plotted with a positive current density denoting a reduction process and with more negative potentials to towards the right side (i.e. 'Texas' convention).

*Pb Electrodeposition* A stock solution of 15.1 ± 0.3 mM $Pb(ClO_4)_2$ (99.995+%, Sigma Aldrich, *MW* = 424.1 g $mol^{-1}$) was prepared using the pre-treated stock 1.25 M NaOH. Electrodepositions were performed under potentiostatic control. Prior to each experiment, 25 mL of blank 1.25 M NaOH electrolyte was introduced to the cell and a bias was applied for 15 minutes prior to spiking in 5 mL of the as-prepared 15.1 ± 0.3 mM $Pb(ClO_4)_2 \bullet H_2O$ stock dilution, giving a final dilution of 2.5 ± 0.1 mM $Pb(ClO_4)_2$. The applied potential was maintained for another 180 minutes after the $Pb^{2+}$ precursor was spiked in.

*Bi Electrodeposition* $Bi_2O_3$ was prepared utilizing an adapted synthetic method to what was reported by Vivier et al.[19] Synthesis of $Bi_2O_3$ was done by preparing a solution of 9.5 mM $Bi(NO_3)_3$ to 1.25 M NaOH solution at room temperature in a polypropylene centrifuge tube. The precipitated solution was centrifuged and rinsed with nanopure water (Barnsted Nanopure >18.2 MΩ cm) three times before transferring to a glass vial and drying overnight in an oven at 100°C. The final $Bi_2O_3$ salt was placed on benchtop open to air prior to use. For electrodeposition, 24 mL of blank pre-treated 1.25 M NaOH(*aq*) electrolyte was added to the cell, the target bias for electrodeposition was then applied for 15 minutes before spiking in 6 mL solution of 0.98 ± 0.04 mM $Bi_2O_3$ to electrodeposit at a concentration of 0.20 ± 0.01 mM $Bi_2O_3$.The applied potential was maintained for another 180 minutes following the spike.

*Pd Electrodeposition* Stock solutions of either 12.1 ± 0.6 or 1.2 ± 0.1 mM $PdCl_2$ (VWR, ≥ 99.99%) in 1.25 M NaOH solution was prepared for electrodeposition. 25 mL of 1.25 M NaOH(*aq*) solution was added to the electrochemical cell, the target bias for electrodeposition was applied for 15 minutes, and then 5 mL of the stock $PdCl_2$ solution was spiked to yield a final concentration of either 2.0 ± 0.1 mM or 0.2 ± 0.02 mM $PdCl_2$ while continuing the applied bias.

*Mn Electrodeposition* A stock solution of alkaline 120µM $Mn(NO_3)_2$ was prepared by adding 5 µL of 1 mg $mL^{-1}$ of $Mn^{2+}$ in 5% (v/v) $HNO_3$ (Acros Organics, ThermoFisher Scientific) to 1.25 M NaOH(*aq*). Electrodeposition was performed by first applying -1.47 V for 15 minutes in the blank electrolyte and then spiking 5 mL of the stock $Mn^{2+}$ solution to a final concentration

of 20 μM. Electrodeposition was performed for 16.5 hours to produce enough material at the Ga electrode interface for ex-situ characterization (*vide supra*). Experiments with concentrations at the $10^{-3}$ M level were not possible due to substantial precipitation of $Mn(OH)_2$.

*Materials Characterization.* Scanning electron microscopy (SEM) was performed with a JEOL JSM-7800FLV field-emission scanning electron microscope with Schottky-type field-emission electron source to confirm the crystals were successfully isolated and transferred onto the Si substrate while maintaining the original orientation relative to the liquid Ga interface. The same SEM microscope used for imaging was also used for EDS and electron backscattering diffraction (EBSD) analyses. All SEM imaging was collected in back-scattered electron mode. The accelerating voltage for SEM/EDS was 20 keV and 25 keV for EBSD. Manual measurements of the average particle size and particle counting was performed using the Fiji distribution of the open source software ImageJ.[20] EBSD data were collected while on the frozen Ga interface, at a 70-degree tilt via an Oxford NordlysMax$^2$ electron backscatter diffraction system. Indexing of the Kikuchi bands and orientation mapping was performed using the Oxford AztecHKL acquisition software.

Several methods were attempted for TEM analysis, including simple 'touch printing.[21] 'Touch printing' with target solid substrates resulted in the transfer of some particles off the surface of liquid Ga but always with a high coating of liquid Ga, complicating further crystallographic and composition analysis. Instead, TEM samples were prepared by first placing a clean Si wafer section onto a hotplate and slowly heating between 40-60°C while "streaking" the frozen Ga droplet across, allowing the crystals at the immediate interface and a minimal amount of residual Ga to be spread along the substrate for collection or further characterization. The act of freezing did not cause or alter any 'innate' particle morphology, as compared to observations from 'touch transfer'. Samples for cross-sectional TEM analysis were then prepared via FIB lift out and thinning using a Thermo Fisher Helios G4 PFIB UXe with a Schottky Field Emitter electron beam source, inductively coupled Xe Gas plasma ion beam source to avoid Ga contamination from the beam, and a Multichem gas injector. The procedure was performed by first placing a protective carbon layer with approximately 100 nm thickness via electron-beam-assisted chemical vapor deposition (CVD) with a 2 kV accelerating voltage and 13 nA beam current. Following, an ion-beam-assisted CVD (IBA-CVD) of a thick (3-4 μm) Pt:C (80:20 mixture) capping layer at 8.00 kV and 0.10 nA ion beam accelerating voltage and current, respectively, was performed. Trenches of the dimensions 20 μm x 23.5 μm x 20 μm (length x width x depth) were then milled into the Si

substrate above and below the capped portion of the electrodeposited metal crystal using a 30 kV accelerating voltage and 60 nA beam current. An Omniprobe AutoProbe 200 micromanipulator equipped with a standard tungsten probe tip (Ted Pella) was then affixed to the Pt:C cap of the sample via a carbon IBA-CVD weld and subsequently transferred and welded onto a Mo Fib lift-out grid. During ion beam thinning of the electrodeposited metal crystals on the grid, there was poor adhesion with the residual Si substrate and Pt:C cap layers. Pt was used with IBA-CVD to backfill the gaps between the sample and the cap and/or Si substrate in between thinning steps.

TEM characterization was performed immediately following sample preparation to minimize oxidation of the thinned samples. TEM imaging was performed using a Thermo Fisher Talos F200X G2 S/TEM X-FEG with a high-brightness Schottky type field emission gun and Gatan One View bottom mount camera. TEM samples were aligned to a major zone axis by using a double tilt holder and analyzing the Kikuchi bands of the sample. All HR-TEM images were subsequently acquired using bright field conditions, meaning that regions of the structure with heavier atoms should appear darker than that of lighter atoms. Additionally, an approximately 100 nm diameter selected area aperture was used for collecting selected area electron diffraction patterns for each sample.

Grazing incidence X-Ray diffraction was performed using a Rigaku Ultima IV Diffractometer with a 2.2 kW Cu Kα radiation long-fine focus tube and a scintillation count detector. The X-ray tube runs at 40 kV and 44 mA, and the Cu Kα line (wavelength 1.5406 Angstrom) used for excitation was obtained using a Kβ filter. The specimen was placed on a thin stage and aligned with a Z-scan prior to each measurement. The divergence, scattering, and receiving slits were set at 1 mm. The distance from the goniometer rotation axis to the detector was set at 285 mm. A scintillation count detector was used to collect the X-ray signal. Diffraction patterns were collected from $2\theta = 10°$ to 90° with a step size of 0.05° and a counting time of 5 seconds.

**Results.**

*Electrochemical Behavior of Ga in 1.25 M NaOH Electrolyte* The extant literature on Ga electrode/water interfaces suggest that an interfacial oxide is always present[22-23] although the Pourbaix diagram[23] suggests a clean metal/water interface at extreme negative potentials. To ascertain this possibility, the electrochemical behavior of liquid Ga was assessed with a pool electrode housed in a Teflon bowl (**Figure 2a**). In 1.25 M NaOH(*aq*), the open-circuit potential (OCP) of liquid Ga was near -1.47 V vs. Hg/HgO (1.25 M NaOH). Cyclic voltammetric sweeps at

a scan rate of 1 V $s^{-1}$ about this potential denoted a quasi-reversible redox process (**Figure 2b**). A pair of reductive and anodic waves corresponding to $8x10^{-2}$ and $-1x10^{-1}$ C $cm^{-2}$, respectively, were noted, corresponding to an oxide coverage of 2 x $10^{-7}$ mol $cm^{-2}$ (i.e. ~ 100 nm thick, assuming a stoichiometry consistent with $Ga_2O_3$). Biasing the Ga electrode just negative of OCP resulted in a slight residual cathode current of -3.1 ± 0. 3 μA $cm^2$ (**Figure 2c**). Conversely, stepping the potential to -1.3 V induced a large anodic current that persisted for 3 min before decaying towards zero. The decay towards zero current at -1.3 V suggested an eventual saturation of a thick surface gallium oxide at long times. Overall, these data implied that the Ga interface was likely unavoidably coated with an interfacial oxide at potentials more positive than OCP but possibly free of oxides at potentials more negative than OCP.

Metal electrodepositions were subsequently performed at -1.47 V. All metal cations of interest had standard potentials at much more positive potentials (Supporting Information). The general electrodeposition process for all metals was as follows. The liquid Ga electrode was first held at -1.47 V for 15 min in blank electrolyte 1.25 M NaOH(*aq*). At $t = 0$, an aliquot of metal salt solution was spiked in to reach a solution concentration of either 2.5 mM ($Pb^{2+}$), 0.2 mM ($Pd^{2+}$ or $Bi^{3+}$) or 2 μM ($Mn^{2+}$), with the concentration of the latter metal cations limited by substantially lower solubility. In all cases at these concentrations, the current changed initially and then attained a non-zero steady-state (cathodic) value (**Figure 2d-g**). Despite varying concentrations of metal pre-cursors being used, the amount of charge passed was maintained within an order of magnitude. Specifically, the charges passed were 0.4 ± 0.1, 0.9 ± 0.4, 1.8 ± 0.4, and 2.0 ± 0.4 C $cm^{-2}$ for the electrodeposition of Bi, Pd, Mn, and Pb, respectively. Separately, each current transient exhibited a noticeable level of noise, with the metals more active towards $H_2$ evolution eliciting more noise in the data.

Physically, the liquid Ga surface largely retained a shiny, mirror-like appearance. Notably, these current-time transients also lacked local maxima at long times (> 1 min) typical of either progressive or instantaneous nucleation at solid surfaces.[24] Local maxima were observed within the first 4 seconds after spiking in the metal salt precursor (Supporting Information). For comparison, control experiments were performed for Pb electrodeposition with liquid Ga electrodes biased at -1.3 V (**Figure 2d**, blue trace). These current-time transients differed, exhibiting a local maxima at long times consistent with electrodeposition at a solid surface. In

these control experiments, copious dark dendrites formed on the surface, accumulating and then spilling over the side of the Teflon bowl. Corresponding elemental analysis indicated a large oxygen signal at the underlying Ga interface, consistent with the presence of an oxide present during Pb electrodeposition under this condition (Supporting Information).

For electrodeposition experiments performed at -1.47 V, the surfaces of the liquid Ga electrodes were examined by scanning electron microscopy (SEM). Upon termination of each experiment, the electrolyte was quickly removed, and the Ga liquid metal droplet was rinsed with copious water (Barnsted Nanopure >18.2 MΩ cm) to remove any excess salts. Flash freezing with liquid nitrogen was then performed to solidify the electrode surface without disturbing the particle orientation. The surfaces of the frozen Ga electrodes were then evaluated by SEM.

In all instances, these samples were devoid of dendrites. Instead in each case, the liquid metal surface was decorated with flat, thin (< 500 nm), metallic, and micron-wide particles (**Figure 3a-d**). The specific profile of these particles varied from discrete triangles and irregular coalesced shapes (Pb electrodeposition), triangles and straight parallel/coalescing lines (Bi electrodeposition), squares (Pd electrodeposition), and hexagons (Mn electrodeposition). Elemental analyses for each particle type confirmed that these structures were neither oxides nor composed of extraneous metals (**Figure 3a-d** insets).

Pb, Pd, and Bi electrodeposition experiments yielded similar particle coverages of ~ 0.3 ± 0.2 $cm^{-2}$ , as estimated by SEM. The average side lengths for Pb triangular particles were 8 ± 8 μm ($N$ = 203) and for Bi triangular particles were 2 ± 2 μm ($N$ = 218). The square particles produced through Pd electrodeposition had average side lengths of 14 ± 13 μm ($N$ = 187). The overall high coverage resulted in many areas of overlapping particles. Mn electrodeposition experiments consistently yielded much lower non-uniform particle coverage of (0.10 ± 0.05 $cm^{-2}$). The electrodeposition of Mn formed hexagonal particles with an average side length of 9 ± 3 μm ($N$ = 12).

Transmission electron microscopy (TEM) was separately performed on the materials produced from each of these electrodepositions. Initial TEM sample preparation was attempted via 'touch printing'[21] a carbon-coated copper TEM grid to the liquid metal interface following electrodeposition. However, subsequent scanning electron microscopic imaging of the copper grids showed no instances of transfer of clean particles without a coating of liquid metal. Rather,

the TEM grids featured an intolerably large amount of liquid Ga and Ga oxides (Supporting Information). Accordingly, samples for transmission electron microscopic analysis were instead prepared after first freezing the bulk liquid metal, then slightly warming each frozen Ga droplet to melt the outer surface, and then streaking the surface across a clean Si wafer substrate. This approach transferred the crystals and limited liquid Ga to the solid substrate without perturbing the original orientation with respect to the liquid metal surface plane. Focused ion beam (FIB) milling was used to cut, to thin, and to lift out a cross section from each particle type (Supporting Information). These thinned sections were then welded to a grid and analyzed by scanning transmission electron microscopy (TEM, **Figure 3e-h**). For these analyses, arbitrary triangular particles after Pb electrodeposition, square particles after Pd electrodeposition, and hexagonal particles after Mn electrodeposition were chosen since these morphologies constituted of 100% of the discrete particles observed in each case. For analysis of products from Bi electrodeposition, lines were the predominant (~75%) morphology but with evidence that the lines initiated and/or terminated at the vertex of triangle particles. Accordingly, we selected these minority morphologies for analysis.

In each case, bright field high resolution imaging (HR-TEM) was performed, with the plane of the image corresponding to the red plane indicated in the inset, i.e. orthogonal to the plane of the liquid metal electrode. For Pb, the real space image (**Figure 3e**) and the corresponding reciprocal space image (**Figure 3i**) of the particles were consistent with a cubic lattice structure where the [111] direction was perpendicular to the liquid metal surface (and parallel to the image plane). Wider field of view selected-area-electron-diffraction (SAED) data corroborated this assignment of the crystal orientation (**Figure 3m**). In the case of Pb, a polycrystalline ring was also visible in the SAED data, arising from PbO produced by the rapid oxidation of the sample in area following FIB thinning. The corresponding data for Bi particles (**Figure 3f, j, n**) indicated the rhombohedral lattice structure but otherwise similar conclusions, i.e. single crystals with an identifiable orientation where the [0001] direction was orthogonal to the liquid metal surface plane. The Bi structure can be described and indexed as rhombohedral, pseudocubic or hexagonal,[25] but we note that this work adopts the hexagonal (hkil) Miller-Bravais notation of rhombohedral (R-3MH) Bi to avoid any ambiguity. Further, the SAED data for all Pb and Bi particles yielded lattice constants consistent with pure metal particles ($a = b = c = 0.495$ nm for Pb[26] and $a = b = 0.455$ nm and $c = 1.19$ nm for Bi[27]), suggesting negligible incorporation of Ga.

For Pd and Mn electrodepositions, the products were similarly single-crystalline. The real space (**Figure 3g**) and reciprocal space (**Figure 3k**) HR-TEM particles produced from Pd electrodeposition were consistent the tetragonal lattice structure of $PdGa_5$. This composition was confirmed by SAED data (**Figure 3o**), where lattice constants consistent with stoichiometric $PdGa_5$ were obtained (i.e. $a = b = 0.645$ nm, and $c = 1.00$ nm). Separate scanning TEM energy dispersive X-ray (STEM-EDX) analyses further supported this assignment (Supporting Information). The orientation of the $PdGa_5$ particles were consistent with the [001] direction normal to the surface plane of liquid Ga. Separately, the real space (**Figure 3h**) and reciprocal space (**Figure 3l**) HR-TEM images of particles produced during Mn electrodeposition suggested cubic $MnGa_4$ as the sole products. This composition was confirmed by corresponding SAED data (**Figure 3p**) which yielded lattice constants (i.e. $a = b = c = 0.559$ nm) consistent with pure $MnGa_4$ and STEM-EDX data (Supporting Information). These particles were consistently oriented with the [111] vector perpendicular to the surface plane of the liquid Ga electrode.

To separately confirm the orientation and to assess the effects of applied potential and concentration on the crystal orientation, grazing incidence X-ray diffraction was performed on undisturbed, frozen Ga surfaces (**Figure 4**). The products from Pb and Pd electrodepositions were more amenable for these studies since the lower concentrations required for Bi and Mn electrodepositions resulted in less total material collected, severely limiting the attainable signal-to-noise in the diffraction data. In these cases, electron back scatter diffraction were attempted to corroborate the orientation assignments (Supporting Information). Electrodeposition of Pb performed at -1.47 V exhibited only a single peak for the (111) plane (**Figure 4a**), in accord with the premise of preferred orientation inferred from the HR-TEM images and electron diffraction. In contrast, experiments performed at -1.30 V exhibited X-ray diffraction peaks at $2\theta = 31.3°$, 36.3°, 52.3°, 62.2°, and 65.3°, indexed to the (111), (020), (220), (311), and (222) planes, respectively. The relative intensities of these signals was in accord with randomly oriented, polycrystalline Pb.[28]

$PdGa_5$ with a predominant orientation was evident in the X-ray diffraction data collected from experiments performed at -1.47 V at low concentrations but not at high concentrations (**Figure 4b**). Specifically, at low concentrations the family of {001} diffraction peaks (i.e. (002), (004), and (006)) were evident, with the signal for the (002) direction at $2\theta = 17.7°$ as

overwhelmingly the most intense. Additional peaks appeared at $2\theta$ = 19.4°, 27.6°, 32.2°, 35.9°, 39.5°, 41.1°, 44.3°, and 55.0° indexed to the (110), (200), (121), (004), (220), (114), (310), and (006) planes, respectively. Although the (001) diffraction signal was not visible in the tetragonal lattice because of the $2_1$ screw axis in this lattice type,[29] the observation of the dominant (002) signal was consistent with the [001] direction as normal to the liquid metal surface plane since they belong to the same family of directions. The appearance of other directions in **Figure 4b** as minor peaks was attributed to the difficulty of obtaining frozen liquid metal surfaces with absolutely no curvature. Increasing the precursor concentration by a factor of 10 resulted in the appearance of several additional peaks with dramatically different relative intensities. The overall pattern of peaks in this case was consistent with a collection of crystallites with randomized orientations with respect to the surface plane of Ga. For Bi electrodeposition (**Figure 4c**), the signal-to-noise was poor but the dominant signal was the diffraction peak along the [0003] direction, consistent with the assigned orientation of the [0001] vector as normal to the liquid metal surface plane.

**Discussion.**

The presented data supports three key points. First, electrodeposition with a preferred orientation can occur at a liquid metal-electrolyte interface without binding agents, additives, or external solid seeding substrates. Second, the orientation of the as-synthesized crystals suggests the crystallographic plane with the highest packing density of atoms is oriented along the surface plane. Third, factors that affect the quasi-epitaxial crystal growth are evident, with the rate of electroreduction and absence of oxides at the liquid metal interface as important. These points are further discussed below.

*Probable Source of Preferred Orientation* All previously reported electrodeposition strategies that produce single-crystalline products utilized at least one of the following four concepts. (*1*) Electrodeposition of a metal layer onto a single-crystalline solid electrode that is epitaxially matched to the desired product film can produce single-crystalline metal films.[30] (*2*) Electrodeposition on a solid electrode with a high lattice mismatch can also yield single-crystalline films if periodic sites between the two materials overlap to form a stable boundary (coincidence site lattice epitaxy).[31-32] (*3*) Initial electrodeposition of a less noble metal crystal on a solid surface followed by controlled galvanic or electrolytic metal replacement with a more noble element can

produce single-crystalline materials with a preferred orientation.[33] (*4*) A chelating/binding reagent in the supporting electrolyte can direct electrodeposition with a preferred orientation through selective adsorption to specific crystallographic planes.[34]

The presented experiments argue against *any* of these four concepts as possible explanations for the directed crystal growth observed here. The possible inclusion of an unintended solid surface within Ga and/or at the Ga/water interface is unlikely. Prior to each electrodeposition, thorough cleaning of both the Teflon components and Ga was performed to mitigate the possibility of macroscopic solid impurities within the cell or electrolyte in every single experiment. The method used to prepare the alkaline electrolyte was sufficient to getter metal impurities as measured by inductively coupled plasma emission (ICP). There was no indication of separate intermetallic crystals from metal impurities separately reacting with Ga in these experiments.

The possible presence and influence of gallenene[35] from surface freezing of Ga is also remote. All electrodepositions were performed intentionally under active heating to ensure the bulk and surface of Ga were molten. Additionally, previous studies demonstrated gallenene could only be prepared and retrieved from a liquid Ga interface with an external solid seed.[35] To date, there are no reports of spontaneous gallenene formation through surface freezing at elevated temperatures. Additionally, although solid gallenene could conceivably promote directed growth for some materials through coincidence site lattice epitaxy, it is improbable that this mechanism is equally operative for all four crystal types shown here.

The data also rule out the possibility of an appreciable gallium oxide serving as a solid nucleating surface in metal electrodeposition at more negative potentials in this electrolyte. The presented data show no accumulation of gallium oxides at the liquid Ga/electrolyte interface at -1.47 V, in agreement with the reported Pourbaix diagram for Ga/water contacts at standard temperature and pressure.[23] Although the limited sensitivities of scanning electron microscopy and energy dispersive spectroscopic measurements allow for the possibility of an ultra-thin gallium oxide film, its hypothetical importance is also likely negligible. Interfacial gallium oxide layers are uniformly amorphous or poorly crystalline.[36-38] Accordingly, consistent and complete lattice matching with Pb, Bi, $PdGa_5$, and $MnGa_4$ so as to seed the systematic growth of each material along specific directions is without precedent. Rather, a gallium oxide would most likely just increase the probability of nucleation but without any preferred orientation or direction (**Figure**

**5a**). The data collected at -1.30 V where an interfacial gallium oxide is clearly present and polycrystalline dendritic growth is observed (Supporting Information) is in line with this premise. Although acidic electrolytes may also be useful in removing surface oxides, alkaline conditions are preferrable to minimize the competition with $H_2$ evolution at the employed negative potentials.

Since the electrolyte had no additional additives, the only species of relevance were the supporting counter ions. There is precedent for chemisorbed ions directing electrochemical inorganic crystal growth at a liquid metal/electrolyte contact.[39-40] Chemisorption of halides to the Hg/water interface was previously used to sequester $Pb^{2+}$ released anodically from Hg-Pb amalgams at positive potentials. The halides coordinated with the $Pb^{2+}$ emitted from the Hg interface. The initial adlayer seeded the oriented growth of larger crystals extending into bulk water.[40] However, the halides in that work were strongly bound to the liquid metal amalgam surface. Additionally, the halides acted as reactants with leached metal cations and eventually were constituent species in the eventual crystal. Neither aspect is relevant to the work shown here. The perchlorate and hydroxide anions have significantly weaker binding affinity for Ga than Ga, with perchlorates generally regarded as the least Lewis basic of all common electrolyte anions.[41-42] Neither perchlorate nor hydroxide appeared in any detectable quantity in the collected metallic crystals.

*Origin of Preferred Orientation* The primary observations of this work are consistent with the premise that liquid Ga itself is imparting directionality to the resultant crystals. In the dilute liquid metal Ga-Pb and Ga-Bi alloys formed by electrodeposition, segregation of the Pb and Bi components occurs since neither solute is miscible with liquid Ga.[43] That is, as soon as appreciable levels of Pb and Bi are introduced, the liquid metal mixtures self-segregate into a solute-rich surface surrounding a Ga-rich bulk. This point is well-established in the behavior of these same liquid alloys when heated and then cooled under vacuum.[9-10, 43-45]

As long as the solute-rich surface remains molten (i.e. either at high temperatures when the composition is held constant or at short times during isothermal electrodeposition), the solute-rich surface attains a nearly close-packed, hexatic structure.[9-10] Based on prior X-ray reflectivity studies,[4-6, 8, 46] the atomic layering extends from the solute-rich surface to the near-surface region of the bulk since both are in contact with dissimilar materials. When the solute-rich surface attains a sufficiently high solute concentration for nucleation (i.e. either at cold temperatures when the

composition is held constant or at long times during isothermal electrodeposition), thin (~25 Å) nuclei form across the solute-rich surface layer. If nucleation occurs without substantial nuclear rearrangement, the most probable structure of these nuclei must be two-dimensional sheets with a high atomic density (**Figure 5b**). Within the two pure metal lattices, the Pb(111) and Bi(0001) planes have the highest in-plane atomic packing density, respectively.[47] The crystal faces parallel to the liquid metal surface were conclusively identified as these specific planes.

Electrodepositions of Pd and Mn shared this same principal observation. In both resultant intermetallic compounds, the product crystals were again oriented in a manner consistent with the planes featuring the highest atomic densities being coincident with the surface plane of the liquid metal. In both of these metal electrodepositions, the presence of a surface-segregated, solute-rich phase separated from the Ga-rich bulk was unlikely. Both Pd and Mn are miscible with liquid Ga. Accordingly, the Pd and Mn solutes were likely instantly and fully solvated by Ga upon dissolution into the liquid metal. Nuclei with a consistent structure (and subsequent crystal growth with a preferred orientation) would still be possible if the following two points were true (**Figure 5c**). First, introduction of the electrodeposited metal solute does not destroy the atomic layering within liquid Ga. This point implies that the solvation shell around each metal solute near the liquid metal/water interface would resemble the atomic layering of liquid Ga. Second, if nucleation again occurs without substantial nuclear rearrangement, the most probable structure for nuclei would be two-dimensional sheets of solutes with a similar arrangement of solvated Ga atoms. This latter point is analogous to the condition for the observation of Pb and Bi crystals with preferred orientation but also requires that the structure of the nuclei specifically mirror the atomic arrangement of the lattice plane with the highest atomic densities of Ga in the resultant intermetallic.

Both intermetallic crystal structures are more complex than the close-packed face centered cubic and rhombohedral motifs of Pb and Bi, respectively. In the $PdGa_5$ lattice, the {001} family of planes has the highest atomic packing density. When viewed along a perpendicular axis, the {001} planes consist of pure Ga and Pd sheets (Supporting Information). The atomic densities of the two distinct Ga sheets combine to a packing density of 0.072 atom $Å^2$. An analogous analysis for $MnGa_4$ (Supporting Information) similarly indicates that the orientation of the crystal has sub-planes of Ga atoms that sum up to an atomic packing density of 0.076 atoms $Å^2$. These packing

densities are consistent with a hypothetical initial Ga atomic layer where each atom has 5 in-plane nearest neighbors (Supporting Information). The prevalence of five-fold, in-plane coordination in the atomic layering within a simple liquid metal (Pb) interface has been predicted and observed previously.[48] It is unclear if five-fold coordination should be expected for Ga (a more covalent liquid metal)[49] but the data presented here suggest this possibility. More broadly, the preferred orientations of both the Pd and Mn intermetallic crystals are consistent with the premise that the structure of the initial nuclei follow the stratified atomic arrangement of the near-surface region of liquid Ga.

*Factors that Prevent 'Quasi-Epitaxial' Crystal Growth in Electrodepositions with Liquid Metal Electrodes* The experiments performed here highlight an aspect that prevents 'quasi-epitaxial' crystal growth in electrodepositions with liquid metal electrodes. Quasi-epitaxial electrodeposition was only observed when the introduction of solute to the liquid metal by electroreduction was sufficiently slow. We found that controlling the precursor concentration in solution was the most effective system property in limiting the reaction flux. As long as the precursor concentrations were kept below a minimum concentration, the resultant crystals exhibited quasi-epitaxy. For Pb and Pd, these concentrations were determined to be 0.2 mM and 2.5 mM, respectively. The monodispersity of the particle morphology depended much more critically on time, where short times (< 180 min) produced singular particle shapes, at the expense of lower total particle densities. It is not clear from these data if the atomic ordering within the near-surface region of the liquid metal was compromised during the timescale of nucleation, the prevalence of secondary nucleation on the nascent crystals started to outpace nucleation in the liquid metal, or both. Nevertheless, additional experiments that reveal both the atomic structure and dynamics at these liquid metal interfaces would be informative on this front and to identify *apriori* the optimal time and concentration points for any liquid metal-metal cation electrodeposition combination.

Additionally, the experiments here, in conjunction with the aforementioned reports on surface freezing of liquid metal alloys, highlight factors that are not determinative in the synthesis of single-crystals with a preferred orientation in liquid metals. The electrodeposition experiments performed here were at ambient pressure and constant temperature. The majority of reports on crystal growth by surface freezing of liquid metals are in vacuum and with deliberate temperature

changes. Accordingly, we interpret these aspects as not critical to the orientation of the resultant crystals.

Separately, the electrodeposition experiments here resolve a subtle disagreement in the surface freezing literature. In surface freezing experiments, the continued growth of large crystals is generally not possible with dilute alloys since the mole fraction of the solute is finite and kept constant. Nevertheless, large single-crystals have been predicted[44] if a sufficient supply of solute and fast diffusional transport were maintained. A competing hypothesis[44] alternatively suggested that instantaneous spinodal phase separation should always occur at liquid metal surfaces, which would result in macroscopic crystals with no preferred orientation. The observations reported here are consistent with the former prediction.

Finally, the possible implications of the term 'quasi-epitaxy' merit mention. Although the orientation of the single crystals shown here strongly support the contention that the liquid metal structure influences nucleation, the data are agnostic to whether the atomic structure of the liquid metal affects crystal growth. The observed crystal morphologies were all consistent with crystal growth occurring faster along planes with higher surface energies, i.e. to maximize the area of the facet with the lowest surface energy.[50-51] Similarly, there was no obvious in-plane ordering of any crystallites along the surface of undisturbed liquid metal electrodes. This point is in strong contrast to observations of crystallites nucleated and grown by conventional epitaxy on a single-crystalline solid substrate,[32] but is fully in line with the structural features of a liquid metal. Since there is no evidence of a long-lived, long-range, in-plane ordering across the surface of a liquid metal/water interface, there should be no expectation of correlated in-plane crystallite orientations. This point was manifested in the experiments with Pb, Pd, and Mn electrodeposition. The peculiar straight parallel lines along the $[11\bar{2}0]$ growth direction observed in the Bi electrodeposition experiments were consistent with prior reports of conventional epitaxial growth of Bi on solid surfaces.[52-54] Further examination of this system is warranted to determine what factor(s) produced these features.

**Conclusions.**

This work introduces the concept of 'quasi-epitaxial' electrodeposition on liquid metal surfaces, i.e. the atomic layering within liquid metal electrodes effects non-random nuclei structures which lead to preferred orientation in electrodeposited crystals. Quasi-epitaxy occurs

without any external solid seed and occurs in ambient, aqueous media. The presented data suggest that the initial nuclei have a structure influenced by the atomic packing in the near-surface layers within Ga. Although the presented data highlight the quasi-epitaxial principle on the formation of known phases and polymorphs, this work opens the possibility that quasi-epitaxy of new phases and crystalline structures may be obtained by electrodeposition at liquid metal electrode interfaces. Specifically, the unique solvation environment of liquid metal interfaces could facilitate structures not known in bulk phase diagrams, as has already been noted in some liquid metal systems.[55-56] Further interrogation of liquid metal/liquid electrolyte interfaces with atomic specificity and fast temporal resolution would be helpful to better clarify the details concerning crystal growth.

**Acknowledgements.**

S. M. recognizes generous support from the National Science Foundation (# 2106315). The authors acknowledge the University of Michigan College of Engineering for financial support and the Michigan Center for Materials Characterization for use of the instruments and staff assistance. The authors also thank Dr. Z. Li for assistance with X-Ray diffraction sample alignments for data collection.

## References.


1. Mauk, M.; Capper, P., Liquid Phase Epitaxy of Electronic, Optical, and Optoelectronic Materials. Wiley: 2007.
2. Liquid Metal as a New Reaction Medium. In *Liquid Metals*, 2022; pp 153-215.
3. Murphy, B. M.; Festersen, S.; Magnussen, O. M., The Atomic scale structure of liquid metal–electrolyte interfaces. *Nanoscale* **2016,** *8* (29), 13859-13866.
4. Elsen, A.; Murphy, B. M.; Ocko, B. M.; Tamam, L.; Deutsch, M.; Kuzmenko, I.; Magnussen, O. M., Surface layering at the mercury-electrolyte interface. *Phys Rev Lett* **2010,** *104* (10), 105501.
5. Regan, M. J.; Kawamoto, E. H.; Lee, S.; Pershan, P. S.; Maskil, N.; Deutsch, M.; Magnussen, O. M.; Ocko, B. M.; Berman, L. E., Surface Layering in Liquid Gallium: An X-Ray Reflectivity Study. *Phys. Rev. Lett.* **1995,** *75* (13), 2498-2501.
6. Magnussen, O. M.; Ocko, B. M.; Regan, M. J.; Penanen, K.; Pershan, P. S.; Deutsch, M., X-ray reflectivity measurements of surface layering in liquid mercury. *Phys Rev Lett* **1995,** *74* (22), 4444-4447.
7. Regan, M. J.; Pershan, P. S.; Magnussen, O. M.; Ocko, B. M.; Deutsch, M.; Berman, L. E., X-ray reflectivity studies of liquid metal and alloy surfaces. *Phys. Rev. B* **1997,** *55* (23), 15874-15884.
8. Shpyrko, O.; Fukuto, M.; Pershan, P.; Ocko, B.; Kuzmenko, I.; Gog, T.; Deutsch, M., Surface layering of liquids: The role of surface tension. *Phys. Rev. B* **2004,** *69* (24), 245423.
9. Yang, B.; Gidalevitz, D.; Li, D.; Huang, Z.; Rice Stuart, A., Two-dimensional freezing in the liquid–vapor interface of a dilute Pb:Ga alloy. *Proc. Nat. Acad. Sci. USA* **1999,** *96* (23), 13009-13011.
10. Li, D.; Jiang, X.; Yang, B.; Rice, S. A., Phase transitions in the liquid-vapor interface of dilute alloys of Bi in Ga: New experimental studies. *J. Chem. Phys.* **2005,** *122* (22), 224702.
11. Cahn, J. W., Critical point wetting. *J. Chem. Phys.* **2008,** *66* (8), 3667-3672.
12. Ebner, C.; Saam, W. F., New reentrant wetting phenomena and critical behavior near bulk critical points. *Phys. Rev. Lett.* **1987,** *58* (6), 587-590.
13. Fahrenkrug, E.; Maldonado, S., Electrochemical Liquid–Liquid–Solid (ec-LLS) Crystal Growth: A Low-Temperature Strategy for Covalent Semiconductor Crystal Growth. *Acc. Chem. Res.* **2015,** *48* (7), 1881-1890.
14. Wu, H.; Hazelnis, J. P.; Maldonado, S., Understanding and Expanding the Prospects for Electrosynthesis with Liquid Metal Electrodes. *Acc. Chem. Res.* **2023,** *56* (7), 846-855.
15. Demuth, J.; Fahrenkrug, E.; Ma, L.; Shodiya, T.; Deitz, J. I.; Grassman, T. J.; Maldonado, S., Electrochemical Liquid Phase Epitaxy (ec-LPE): A New Methodology for the Synthesis of Crystalline Group IV Semiconductor Epifilms. *J. Am. Chem. Soc.* **2017,** *139* (20), 6960-6968.
16. Downes, N.; DeMuth, J.; Waelder, J.; Cheek, Q. B.; Bartels, H.; Maldonado, S., Si Electrochemical Liquid Phase Epitaxy: Low-Temperature Growth of Hyperdoped Epitaxial Si Films. *Chemistry of Materials* **2022,** *34* (24), 10861-10872.
17. Márquez, R. A.; Kawashima, K.; Son, Y. J.; Castelino, G.; Miller, N.; Smith, L. A.; Chukwuneke, C. E.; Mullins, C. B., Getting the Basics Right: Preparing Alkaline Electrolytes for Electrochemical Applications. *ACS Energy Letters* **2023,** *8* (2), 1141-1146.
18. Hurlen, T.; V»land, T.; Lunde, G., Anodic dissolution of liquid gallium. *Electrochimica Acta* **1964,** *9* (11), 1433-1437.
19. Vivier, V.; Régis, A.; Sagon, G.; Nedelec, J. Y.; Yu, L. T.; Cachet-Vivier, C., Cyclic voltammetry study of bismuth oxide Bi2O3 powder by means of a cavity microelectrode coupled with Raman microspectrometry. *Electrochimica Acta* **2001,** *46* (6), 907-914.
20. Schindelin, J.; Arganda-Carreras, I.; Frise, E.; Kaynig, V.; Longair, M.; Pietzsch, T.; Preibisch, S.; Rueden, C.; Saalfeld, S.; Schmid, B.; Tinevez, J.-Y.; White, D. J.; Hartenstein, V.; Eliceiri, K.; Tomancak, P.; Cardona, A., Fiji: an open-source platform for biological-image analysis. *Nature Methods* **2012,** *9* (7), 676-682.

21. Zavabeti, A.; Ou, J. Z.; Carey, B. J.; Syed, N.; Orrell-Trigg, R.; Mayes, E. L. H.; Xu, C.; Kavehei, O.; O'Mullane, A. P.; Kaner, R. B.; Kalantar-zadeh, K.; Daeneke, T., A liquid metal reaction environment for the room-temperature synthesis of atomically thin metal oxides. *Science* **2017,** *358* (6361), 332-335.
22. Hong, B.; Wang, Y.; Wei, X.; Huang, Q.; Wang, X.; Fujita, T.; Wei, Y., EQCM study on the electrochemical redox behavior of gallium in alkaline solution. *Hydrometallurgy* **2020,** *194*, 105344.
23. Chung, Y.; Lee, C.-W., Electrochemistry of Gallium. *J. Electrochem. Sci. Technol* **2013,** *4* (1), 1-18.
24. Milchev, A.; Krastev, I., Two-dimensional progressive and instantaneous nucleation with overlap: The case of multi-step electrochemical reactions. *Electrochimica Acta* **2011,** *56* (5), 2399-2403.
25. Hofmann, P., The surfaces of bismuth: Structural and electronic properties. *Progress in Surface Science* **2006,** *81* (5), 191-245.
26. Swanson, H. E.; Tatge, E.; United States. National Bureau of, S., *Standard X-ray diffraction powder patterns. Vol. I, Data for 54 inorganic substances*. National Bureau of Standards: [Washington, D.C.], 1953; Vol. [Washington, D.C.].
27. Pilloni, M.; Ennas, G.; Cabras, V.; Denotti, V.; Kumar, V. B.; Musinu, A.; Porat, Z.; Scano, A.; Gedanken, A., Thermal and structural characterization of ultrasonicated BiSn alloy in the eutectic composition. *Journal of Thermal Analysis and Calorimetry* **2015,** *120* (3), 1543-1551.
28. Gontad, F.; Lorusso, A.; Klini, A.; Loufardaki, A.; Panareo, M.; Fotakis, C.; Perrone, A., Picosecond and subpicosecond pulsed laser deposition of Pb thin films. *Physical Review Special Topics - Accelerators and Beams* **2013,** *16* (9), 093401.
29. Nespolo, M., International Tables for Crystallography, Volume A, Space-group symmetry. Edited by Mois I. Aroyo. Wiley, 2016. ISBN 978-0-470-97423-0. *Acta Crystallographica Section A: Foundations and Advances* **2017,** *73* (3), 274-276.
30. Möller, F. A.; Magnussen, O. M.; Behm, R. J., Electrodeposition and Anodic Dissolution of Ni on Au(100): an in situ STM Study*. *Zeitschrift für Physikalische Chemie* **1999,** *208* (1-2), 57-75.
31. Hull, C. M.; Switzer, J. A., Electrodeposited Epitaxial Cu(100) on Si(100) and Lift-Off of Single Crystal-like Cu(100) Foils. *ACS Applied Materials & Interfaces* **2018,** *10* (44), 38596-38602.
32. Switzer, J. A.; Liu, R.; Bohannan, E. W.; Ernst, F., Epitaxial Electrodeposition of a Crystalline Metal Oxide onto Single-Crystalline Silicon. *The Journal of Physical Chemistry B* **2002,** *106* (48), 12369-12372.
33. Liang, X.; Zhang, Q.; Lay, M. D.; Stickney, J. L., Growth of Ge Nanofilms Using Electrochemical Atomic Layer Deposition, with a "Bait and Switch" Surface-Limited Reaction. *Journal of the American Chemical Society* **2011,** *133* (21), 8199-8204.
34. Wang, H.; Liang, Z.; Tang, M.; Chen, G.; Li, Y.; Chen, W.; Lin, D.; Zhang, Z.; Zhou, G.; Li, J.; Lu, Z.; Chan, K.; Tan, T.; Cui, Y., Self-Selective Catalyst Synthesis for CO2 Reduction. *Joule* **2019,** *3* (8), 1927-1936.
35. Kochat, V.; Samanta, A.; Zhang, Y.; Bhowmick, S.; Manimunda, P.; Asif, S. A. S.; Stender, A. S.; Vajtai, R.; Singh, A. K.; Tiwary, C. S.; Ajayan, P. M., Atomically thin gallium layers from solid-melt exfoliation. *Science Advances* **2018,** *4* (3), e1701373.
36. Regan, M.; Tostmann, H.; Pershan, P. S.; Magnussen, O.; DiMasi, E.; Ocko, B.; Deutsch, M., X-ray study of the oxidation of liquid-gallium surfaces. *Physical Review B* **1997,** *55* (16), 10786.
37. Plech, A.; Klemradt, U.; Metzger, H.; Peisl, J., In situ x-ray reflectivity study of the oxidation kinetics of liquid gallium and the liquid alloy. *Journal of Physics: Condensed Matter* **1998,** *10* (5), 971.
38. Chabala, J. M., Oxide-growth kinetics and fractal-like patterning across liquid gallium surfaces. *Physical Review B* **1992,** *46* (18), 11346.
39. Festersen, S.; Runge, B.; Koops, C.; Bertram, F.; Ocko, B.; Deutsch, M.; Murphy, B. M.; Magnussen, O. M., Nucleation and Growth of PbBrF Crystals at the Liquid Mercury–Electrolyte Interface Studied by Operando X-ray Scattering. *Langmuir* **2020,** *36* (37), 10905-10915.
40. Sartori, A.; Giri, R. P.; Fujii, H.; Hövelmann, S. C.; Warias, J. E.; Jordt, P.; Shen, C.; Murphy, B. M.; Magnussen, O. M., Role of chemisorbing species in growth at liquid metal-electrolyte interfaces revealed by in situ X-ray scattering. *Nature Communications* **2022,** *13* (1), 5421.

41. Linert, W.; Camard, A.; Armand, M.; Michot, C., Anions of low Lewis basicity for ionic solid state electrolytes. *Coordination Chemistry Reviews* **2002,** *226* (1), 137-141.
42. Davies, J.; Hartley, F., Complexes of the platinum metals containing weak donor ligands. *Chemical Reviews* **1981,** *81* (1), 79-90.
43. Issanin, A.; Turchanin, A.; Freyland, W., Electron spectroscopy and scanning tunneling microscopy study of quasi-two-dimensional freezing at the liquid/vapor interface of Ga-Bi alloys. *J. Chem. Phys.* **2004,** *121* (23), 12005-12009.
44. Huber, P.; Shpyrko, O.; Pershan, P. S.; Ocko, B.; DiMasi, E.; Deutsch, M., Short-range wetting at liquid gallium-bismuth alloy surfaces: X-ray measurements and square-gradient theory. *Phys. Rev. B* **2003,** *68* (8), 085409.
45. Dogel, S.; Nattland, D.; Freyland, W., Complete wetting transitions at the liquid-vapor interface of gallium-bismuth alloys: Single-wavelength and spectroscopic ellipsometry studies. *Phys. Rev. B* **2005,** *72* (8), 085403.
46. Pershan, P. S., X-ray scattering: Liquid metal/vapor interfaces. *The European Physical Journal Special Topics* **2011,** *196* (1), 109-120.
47. Halka, V.; Freyland, W., Thermal stability of surface freezing films in Ga-based alloys: An x-ray photoelectron spectroscopy and scanning tunneling microscopy study. *J. Chem. Phys.* **2007,** *127* (3), 034702.
48. Reichert, H.; Klein, O.; Dosch, H.; Denk, M.; Honkimäki, V.; Lippmann, T.; Reiter, G., Observation of five-fold local symmetry in liquid lead. *Nature* **2000,** *408* (6814), 839-841.
49. Ghigna, P.; Spinolo, G.; Parravicini, G. B.; Stella, A.; Migliori, A.; Kofman, R., Metallic versus Covalent Bonding: Ga Nanoparticles as a Case Study. *J. Am. Chem. Soc.* **2007,** *129* (25), 8026-8033.
50. Li, L.; Goodrich, C.; Yang, H.; Phillips, K. R.; Jia, Z.; Chen, H.; Wang, L.; Zhong, J.; Liu, A.; Lu, J., Microscopic origins of the crystallographically preferred growth in evaporation-induced colloidal crystals. *Proceedings of the National Academy of Sciences* **2021,** *118* (32), e2107588118.
51. Lin, H.; Liu, J.-X.; Fan, H.; Li, W.-X., Compensation between Surface Energy and hcp/fcc Phase Energy of Late Transition Metals from First-Principles Calculations. *The Journal of Physical Chemistry C* **2020,** *124* (20), 11005-11014.
52. Kowalczyk, P. J.; Mahapatra, O.; McCarthy, D. N.; Kozlowski, W.; Klusek, Z.; Brown, S. A., STM and XPS investigations of bismuth islands on HOPG. *Surface Science* **2011,** *605* (7), 659-667.
53. Miki, K.; Owen, J. H. G.; Bowler, D. R.; Briggs, G. A. D.; Sakamoto, K., Bismuth-induced structures on Si(001) surfaces. *Surface Science* **1999,** *421* (3), 397-418.
54. Miki, K.; Bowler, D. R.; Owen, J. H. G.; Briggs, G. A. D.; Sakamoto, K., Atomically perfect bismuth lines on Si(001). *Physical Review B* **1999,** *59* (23), 14868-14871.
55. Shpyrko, O. G.; Streitel, R.; Balagurusamy, V. S.; Grigoriev, A. Y.; Deutsch, M.; Ocko, B. M.; Meron, M.; Lin, B.; Pershan, P. S., Surface crystallization in a liquid AuSi alloy. *Science* **2006,** *313* (5783), 77-80.
56. Mechler, S.; Yahel, E.; Pershan, P. S.; Meron, M.; Lin, B., Crystalline monolayer surface of liquid Au–Cu–Si–Ag–Pd: metallic glass former. *Applied Physics Letters* **2011,** *98* (25), 251915.

**Figures.**

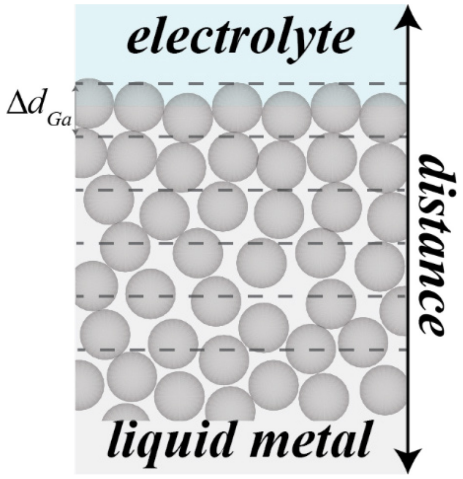


**Figure 1.** Schematic depiction of the short-range in-plane atomic layering in the near surface region of a liquid metal/electrolyte interface which decreases monotonically into the bulk liquid metal. Atomic layers (dashed grey lines) are defined by the diameter of a Ga atom ($\Delta d_{Ga}$) to highlight deviations of the atomic layering as the short-range order behavior trends toward that of a liquid traversing deeper into the bulk away from the electrolyte.

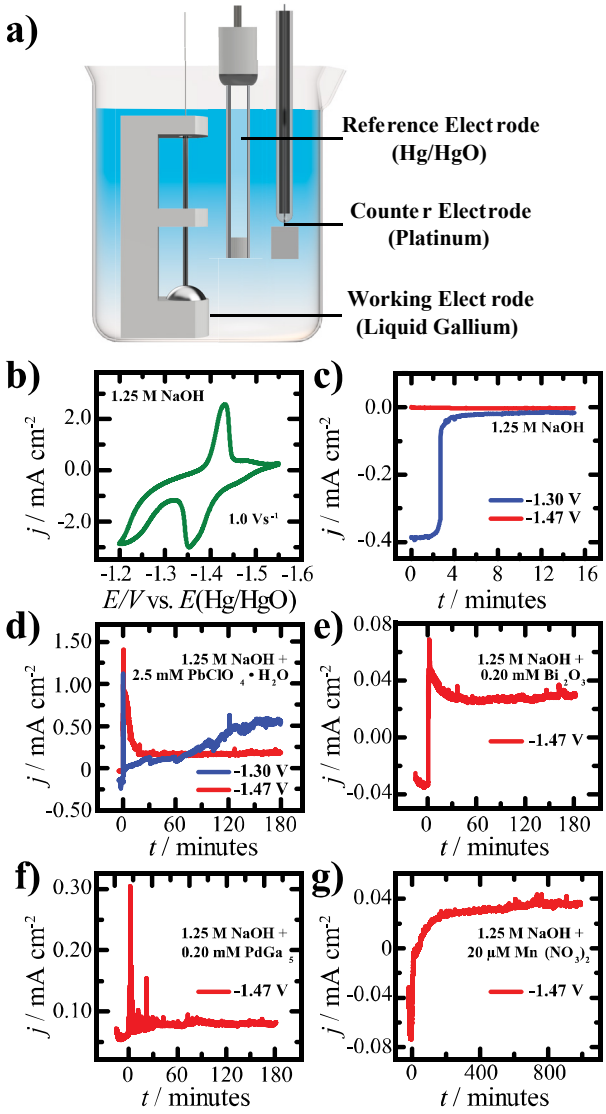


**Figure 2. a)** Schematic depicting the electrochemical cell with a liquid Ga working electrode for electrodeposition and cyclic voltammetry measurements. **b)** Cyclic Voltammetry of a blank 1.25 M NaOH electrolyte in contact with a liquid Ga working electrode at 1.0 V $s^{-1}$. **c)** Current-time transient responses from potential step experiments to (blue) -1.30 V and (red) -1.47 V (red) vs. Hg/HgO (1.25M NaOH) in blank 1.25 M NaOH solution for an initial 15 minutes prior to electrodeposition. **d-g)** Current-time transients for electrodeposition potentials of -1.30 V (blue) and -1.47 V (red) where $t$ = 0 minutes is defined as the time when an aliquot of **d)** 15 mM $PbClO_4$, **e)** 1. 0 ± 0.01 mM $Bi_2O_3$, **f)** 1.20 ± 0.01 mM $PdCl_2$, or **g)** 0.120 mM $Mn(NO_3)_2$ is spiked in.

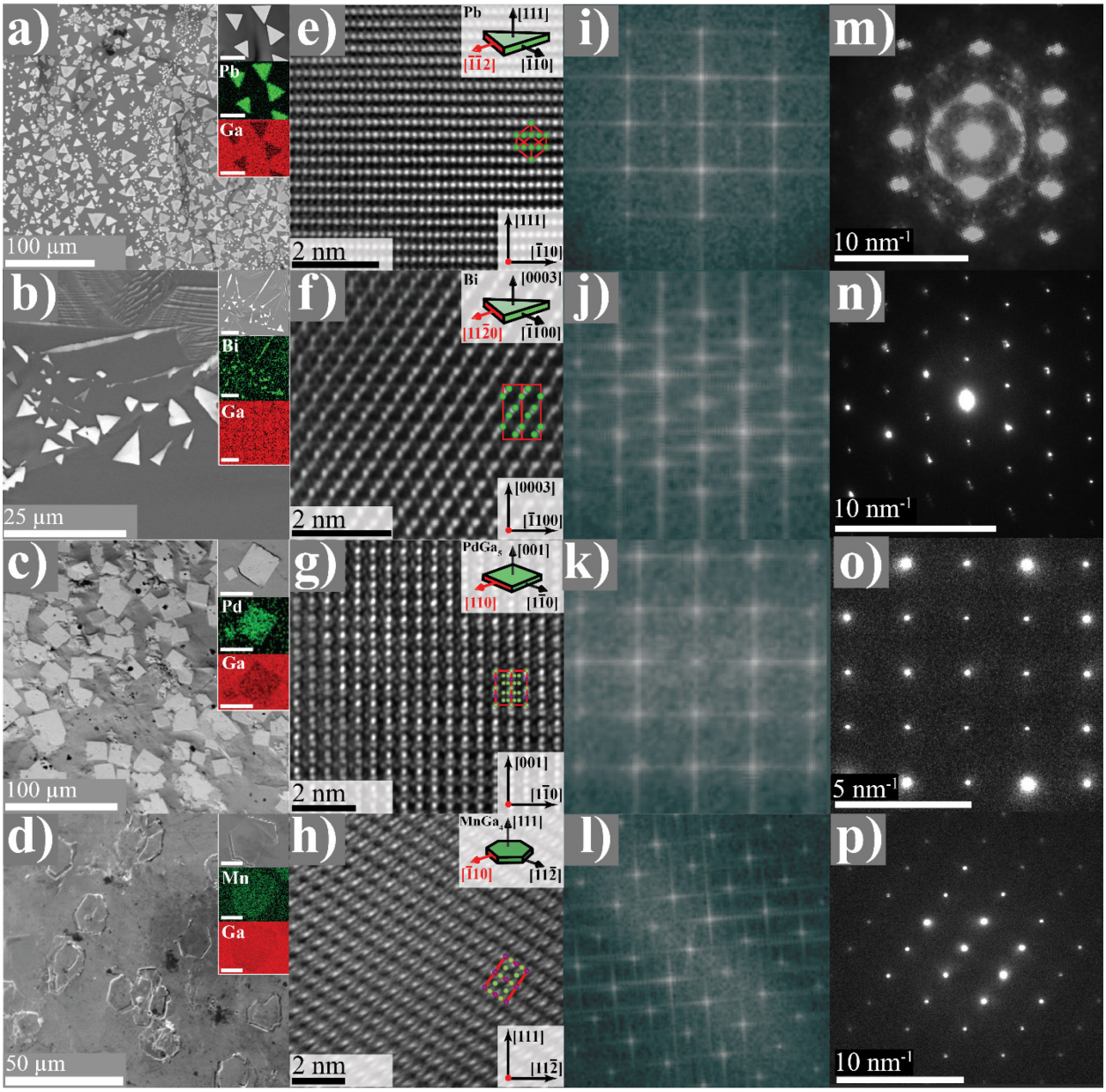


**Figure 3.** SEM and corresponding elemental mapping of the particles produced after metal electrodeposition at -1.47 V including **a)** Pb triangular particles (inset scale bar = 10 µm) **b)** Bi nanoribbons and triangular particles (inset scale bar = 25 µm) **c)** $PdGa_5$ square particles (inset scale bar = 25 µm) **d)** $MnGa_4$ nanoribbons and triangular particles (inset scale bar = 5 µm). Corresponding cross-sectional HR-TEM bright field image of the **e)** [$\bar{1}\bar{1}$2] direction of a Pb triangular particle, **f)** [11$\bar{2}$0] direction of a Bi triangular particle, **g)** [110] direction of a $PdGa_5$ square particle, **h)** [$\bar{1}$10] direction $MnGa_4$ hexagonal particle with the face of the particle probed highlighted in red (inset) and a guiding overlay of the atomic arrangement corresponding to the unit cell viewed in that crystallographic direction for Ga (green) and Pd or Mn (purple). **(i-l)** Corresponding FFT of (e-h) respectively and experimental selected area electron direction for **m)** Pb, **n)** Bi, **o)** $PdGa_5$, and **p)** $MnGa_4$ in the orientation shown in (e-h) respectively.

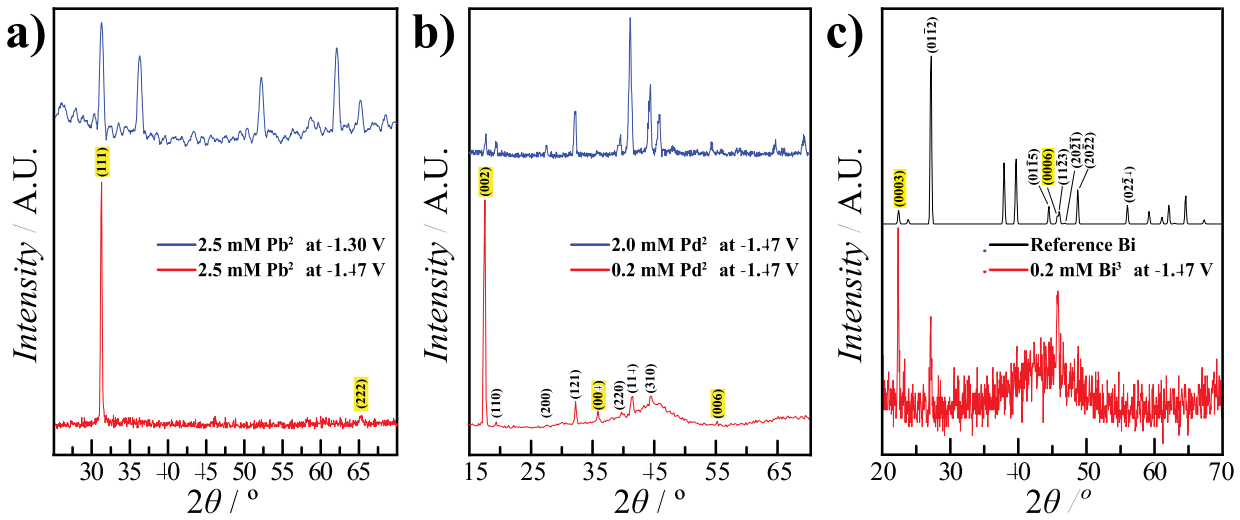


**Figure 4.** Grazing incidence x-ray diffraction data of the Ga electrode interface following electrodeposition in 1.25 M NaOH electrolyte containing either **a)** 2.5 mM $PbClO_4 \bullet H_2O$ at -1.30 V (blue) and -1.47 V (red) with peaks corresponding to the {111} preferred orientation of the deposition product Pb highlighted in yellow, **b)** 2.0 mM $PdClO_4$ (blue) and 0.2 mM $PdClO_4$ (red) with peaks corresponding to the {001} preferred orientation of the deposition product $PdGa_5$ highlighted in yellow **c)** 0.2 mM $Bi_2O_3$ at -1.47 V (red) and corresponding reference XRD spectra for a polycrystalline Bi sample with peaks corresponding to the preferred {0001}orientation of the electrodeposition product Bi highlighted in yellow.

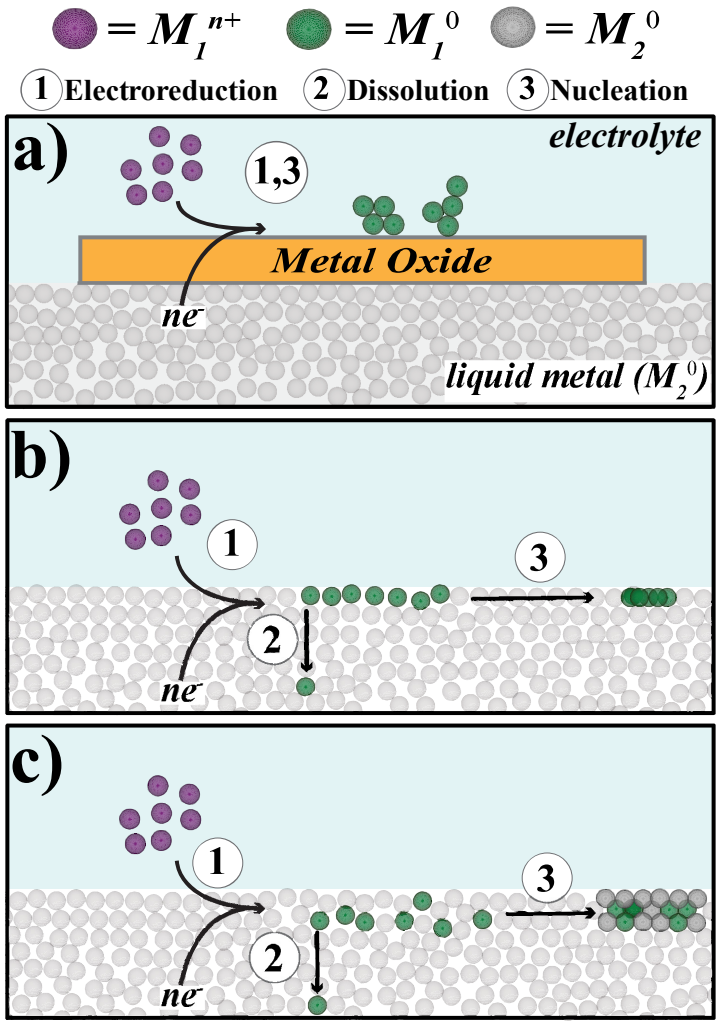


**Figure 5.** Graphical summary of the key electrodeposition steps in nucleus formation by quasi-epitaxy starting with the (*1*) electrochemical reduction of a dissolved metal precursor ($M_1^{n+}$) to achieve one of three observed products: **a)** polycrystalline metal ($M_1^0$) dendrites by heterogeneous nucleation on the solid surface oxide, **b**) single crystalline $M_1^0$ by nucleation of $M_1^0$ via self-segregation at the interface in a close-packed form, or **c)** single crystalline intermetallic via nucleation governed by the in-plane packing of $M_2^0$. In both (b) and (c), a fraction of electrodeposited metal atoms do not participate in nucleation at the interface and will instead dissolve into the liquid metal bulk ($M_2^0$).

**Table of Contents Graphic**